Iron Speciation of Natural and Anthropogenic Dust by Spectroscopic and Chemical Methods

Chiara Petroselli [1,2,*], Beatrice Moroni [1,3], Stefano Crocchianti [1], Roberta Selvaggi [1], Riccardo Vivani [4], Francesco Soggia [5], Marco Grotti [5] and Francesco d'Acapito [6] and David Cappelletti [1,3,7]

1   Dipartimento di Chimica, Biologia e Biotecnologie, Università degli Studi di Perugia, via Elce di Sotto 8, 06123 Perugia, Italy; b.moroni@tiscali.it (B.M.); croc@impact.dyn.unipg.it (S.C.); roberta.selvaggi@unipg.it (R.S.); david.cappelletti@unipg.it (D.C.)
2   CNR-IBIMET, via P. Gobetti 101, 40129 Bologna, Italy
3   SMAArt, Università degli Studi di Perugia, Piazza dell'Università 1, 06123 Perugia, Italy
4   Dipartimento di Scienze Farmaceutiche, Università degli Studi di Perugia, via A. Fabretti 48, 06123 Perugia, Italy; riccardo.vivani@unipg.it
5   Dipartimento di Chimica e Chimica Industriale, Universitá degli Studi di Genova, via Dodecaneso 31, 16146 Genova, Italy; soggia@chimica.unige.it (F.S.); grotti@unige.it (M.G.)
6   CNR-IOM-OGG c/o ESRF LISA CRG, 71 Avenue des Martyrs, F-38043 Grenoble, France; dacapito@esrf.fr
7   CNR-ISAC, via P. Gobetti 101, 40129 Bologna, Italy
*   Correspondence: chiara.petroselli@unipg.it; Tel.: +39-075-585-5530

check for updates

Abstract: In this work, we have characterized the iron local structure in samples of two different types of atmospheric dust using X-ray absorption spectroscopy and selective leaching experiments. Specifically, we have investigated samples of long-range transported Saharan dust and freshly emitted steel plant fumes with the aim of individuating possible fingerprints of iron in the two cases. Findings include (1) prevalence of octahedral coordinated Fe^{3+} for all samples; (2) presence of 6-fold coordinated Fe^{3+}, aluminosilicates and iron oxy(hydr)oxides in Saharan dust and (3) of Fe-bearing spinel-like structures in the industrial fumes; (4) general predominance of the residual insoluble fraction with a notable difference: 69% for Saharan dust and 93% for steel production emissions, associated with aluminosilicates and non-reducible iron oxy(hydr)oxides, and Fe spinels, respectively. The remarkable differences between the X-ray absorption spectroscopy (XAS) spectra and leaching test results for the two sample types suggest the possibility to exploit the present approach in more complex cases. To this aim, two additional case studies of mixed aerosol samples are presented and discussed.

1. Introduction

Airborne iron is widely studied in environmental chemistry because of the implications of its solubility on bioaccessibility. As an illustration, the deposition of desert dust provides the iron fertilization of high-nutrient-low-chlorophyll areas like open oceans [1] and the Amazonian rain-forest [2], despite this is still a debated hypothesis [3]. Moreover, this process promotes the sequestration of CO_2 from the atmosphere [4], exerting an effect on global biogeochemical cycles. On the other side, when desert dust transport affects densely populated areas, it becomes important to assess its impact on local air quality and human health. For example, Stafoggia et al. [5] demonstrated that, even if Saharan dust is classified as a natural aerosol, it affects human health as much as

anthropogenic aerosols because of its elevated mass concentrations. However, deserts are not the only source of airborne iron. For instance, industrial emissions and in particular steel plant fumes also provide significant inputs of atmospheric aerosols which may impact on urban areas. Emitted aerosols typically show a high content of iron, mainly in oxide structures, mixed with other transition metals [6] and they have been proven to exert an adverse impact on human health [7]. Eventually, the solubility of iron in aerosols is the relevant feature for toxicological issues related to the interaction with biological tissues inside the lungs [8].

A detailed understanding of properties such as metal solubility and reactivity is based on the knowledge of the local structure at the atomic level (coordination number, redox state, and speciation). For example, it has been demonstrated that iron solubility in dust is driven by its chemical speciation and mineralogy [9,10]. Moreover, particles size can also play a role [11]. In this frame, the chemical and structural complexity of an atmospheric aerosol matrix may be a challenging obstacle in the determination of these structural parameters. In particular, the abundance and structural characteristics of iron in atmospheric aerosols is highly variable and determined by many different factors. Indeed, spatial and temporal variations in aerosol iron speciation depend critically on the source region and this fact could have a significant effect on aerosol iron solubility. Moreover, iron solubility can change during the permanence of aerosol in the atmosphere, due to atmospheric and cloud processing [12]. As a consequence, iron solubility values reported in the literature range widely from 0.05% to 80% (e.g., Mahowald et al. [13]).

Iron valence state and mineralogy can be characterized using different approaches. These range from classic wet-chemical methods such as ferrozine [14], to Mössbauer spectroscopy [15] and techniques based on synchrotron radiation such as X-ray Absorption Spectroscopy (XAS). Basically, XAS allows to determine the valence state of the metal [16] and to obtain information on the local order, ligands, coordination number and inter-atomic distances [17]. Moreover, XAS can be applied both for bulk and single-particle analyses, and thus provides in principle the possibility to investigate the structural features of minerals in atmospheric aerosols that may impact the environmental biogeochemistry. The complexity of investigating environmental matrices using XAS has been shown by several studies, where this technique has been applied to the characterization of atmospheric aerosols [18,19], and more specifically to urban particulate matter [20–22] and road dust [23]. The study of paleoclimatic archives of mineral dust, such as ice cores, has been achieved by applying an integrated experimental approach described by Marcelli et al. [24], recently applied also by Baccolo et al. [25].

The chemical composition of Saharan dust has been investigated by various techniques [26,27] including XAS methods for iron mineralogy and speciation [28]. Atmospheric processing of Saharan dust has been studied by atmospheric modeling [29] and artificial ageing with a few applications of XAS techniques to these kinds of laboratory experiment [30,31]. In any case, XAS has been used only for samples collected close to the source regions or after short-range transport [28], while no studies are currently available on the characterization of long-range transported Saharan dust, as we have carried out in the present work. Long-range transport is a crucial point since it influences, through atmospheric and in-cloud processes, the redox state, local structure and also the solubility of the particulate matter constituents, including iron. Despite several studies have applied chemical speciation methods to the study of iron and other metals solubility in industrial fumes [32], XAS techniques have been applied so far only to trace metals such as Zn, Cd and Pb [33]. Regarding industrial fumes, XAS and speciation studies on aerosols sampled directly at chimney stacks are limited in the literature [34].

In this work, we applied an integrated experimental approach to the characterization of two different and well-defined iron-bearing aerosol types. In particular, XAS measurements have been complemented with iron bulk determination by the application of a sequential extraction scheme and successive ICP-OES (Inductively Coupled Plasma - Optical Emission Spectroscopy), which allowed us to investigate the iron selective solubility and the influence of the sampling conditions. The two cases under study are (1) Saharan dust collected after a long-range transport at the EMEP regional background site of Monte Martano (Central Italy; [35]) and (2) freshly emitted welding fumes collected

at the chimneys of the TK-Acciai Speciali Terni (AST) steel plant in Terni [36], a historical industrial town located at a short distance from Monte Martano. These two types of atmospheric aerosols which contain enough iron to be speciated with XAS techniques, are expected to have a very different microstructure and mineralogy. Moreover, we carried out the characterization of two additional urban aerosol samples. The first has been collected in Terni during the same Saharan advection sampled at Monte Martano and therefore represents the case of desert dust contaminated by urban aerosol. The second has been taken near the steel plant, in the absence of dust from long-range intrusion. The second example depicts the case of an industrial fume mixed with an urban aerosol. In both cases, we exploited the same experimental techniques as for the previous samples.

2. Materials and Methods

2.1. Sampling Sites

The atmospheric aerosol samples analyzed in this study were collected at four sampling sites in Central Italy: the rural regional background station of Monte Martano (MM) during a very intense Saharan dust outbreak in December 2014 [37], the chimney stack of the steel plant located in Terni (TK-AST ThyssenKrupp) during an intensive sampling campaign in May 2016, and two sites in the Terni urban area. A geographical terrain map of the sites can be found in the Supplementary Material, Figure S1.

MM (1100 m a.s.l.; 42°48'19'' N, 12°33'55'' E; Figure S1a) is a well-suited site for the characterization of long-range transport events such as Saharan dust outbreaks [38] due to its elevation, a completely free horizon and the low impact of local sources. The site is located in the free troposphere for most of the year except for a few daily hours in the summertime [35]. Since 2013 the MM site has been part of the Sand and Dust Storms Warning Advisory and Assessment System (SDS-WAS) network of the World Meteorological Organization.

Terni (130 m a.s.l.; 42°33'58'' N, 12°38'56'' E; Figure S1b) is an industrial city which has been well-known for stainless steel production since XIX century. The city is situated 40 km south of MM and lies in a valley surrounded by mountains which prevent the dispersion of pollutants from local sources such as traffic, domestic heating, and industrial plants [39]. The AST steel plant is in the urban area and has a distinct impact on urban aerosols [36]. The two urban sites chosen for this work are Borgo Rivo, mainly affected by autovehicular traffic emissions, and Prisciano, an urban/industrial site located near the AST steel plant.

2.2. Aerosol Samples Description

An extremely intense Saharan dust outbreak (SDO), which occurred in the Central Mediterranean between 30 November and 1 December 2014, has been taken into consideration. Back trajectories of air masses, computed hourly with HYbrid Single-Particle Lagrangian Integrated Trajectory (HYSPLIT) modeling system ([40]; Figure S2a, Supplementary Material), indicated the clear Saharan provenance. A more detailed analysis of back trajectories, not shown in the figure, revealed that the first-day trajectories were coming from Tunisia and Libya while a transport from Tunisia and Algeria was observed the day after; the air masses travelled at low height above ground level on both days. Because of the massive dust transport and the height of the air masses over the receptor site, as inferred by BTs calculation, the daily PM_{10} concentrations at MM were exceptionally high (Figure S2b, Supplementary Material; Table 1): 83.9 μg m^{-3} on 30 November and 86.9 μg m^{-3} on 1 December, which are far above the average value of 10.1 μg m^{-3} for the whole year (2014). The Saharan dust load was calculated following the procedure suggested by Escudero et al. [41], and it was 83.0 μg m^{-3} on 1 December, accounting for about 96% of the total mass loaded on the filter. During this event, 12 samples were collected on different substrates (quartz fiber, and polycarbonate) using both high-volume (Air HVS flow, Analitica Strumenti, 1140 L/min) and low-volume (SWAM, FAI Instruments, 38.3 L/min and ECHO-PM, Tecora, 38.3 L/min) samplers with PM_{10} and $PM_{2.5}$ size selective impactors. XAS have

been applied to all the samples and the analysis, described in the following sections, shows no substantial differences between filter types and sampling flow rates. Therefore, since the primary goal of the present work is the comparison of Saharan dust with steel plant fumes, we will consider in the discussion only the low volume PM_{10} sample of 1 December 2014 (SH_Dec2014 in the following) for which we employed the same filter type (quartz fiber filter, Whatman QM 47 mm) used for the sampling of the industrial emissions. Despite this advantage, the choice of quartz filter has also some disadvantages including the possible contamination of blanks and the impossibility to estimate accurately the thickness of the deposit due to the fibrous nature of the substrate that allows to aerosol particles to penetrate inside the filter.

Aerosol particles from steel plant emissions were collected at the five main chimney stacks of the TK-AST plant in the Terni city, which correspond to three smelters and two converters. The specific sample discussed in the present paper was collected by an isokinetic sampling of the total suspended particulate matter at the E45 chimney stack at an average flow of 20 L/min for about 4.5 h. The E45 converter was chosen due to its high aerosol loading. The total aerosol mass, determined by gravimetric methods on the aerosol sample (AST_E45 in the following), is 9.12 $\pm$ 0.05 mg which results in 1.7×10^4 μg m^{-3} aerosol mass concentration.

The AST_E45 aerosol sample was taken directly at the chimney stack of the steel plant and therefore provides a direct fingerprint of this specific source. The SH_Dec2014 dust sample was taken at the MM receptor site, after a very long-range transport in the atmosphere. However, the exceptional magnitude of the mass concentration showed a clear dominance of the long-range transport component over the local background portion and this allowed us to consider the SH_Dec2014 sample as a fingerprint of a nearly pure and aged Saharan dust event.

Two more samples were considered in the present work (Table 1). The first sample (TR_mix1) was collected in the urban area of Terni (TR) during the December 2014 SDO. The filter analyzed is the PM_{10} low volume sample of 1 December 2014, collected on the same quartz fiber filter type as the SH_Dec2014 and AST_E45 samples. This intrusion had a considerable effect on the urban aerosol concentration. The PM_{10} value recorded in Terni on the 1 December 2014 reached 109.9 μg m^{-3} and the Saharan dust load, calculated in the same way as for the SH_Dec2014 case, added to 71.2 μg m^{-3}, thereby accounting for 65% of the aerosol mass on the filter. The Saharan dust load registered in Terni is similar to the value recorded at the MM site suggesting a strong contribution of the Saharan dust advection to the urban environment. The second mixed aerosol sample was collected in a different monitoring station of the Terni urban area, which is the nearest to the steel plant, on 1 December 2016 (TR_mix2 in the following). It is a $PM_{2.5}$ sample and its aerosol mass concentration is 62.2 μg m^{-3}, with an iron concentration of 0.17 μg m^{-3}, which accounts for 0.27% of the total mass.

The differences observed in the absolute values of aerosol mass concentration and iron content are also reflected on the iron mass percentage values, reading 1.8% for SH_Dec2014, 13.5% for AST_E45, 2.1% for TR_mix1 and 0.3% for TR_mix2.

The iron content in blank filters was determined by ICP-OES, providing a concentration of 1.43 μg on the entire filter, which corresponds to 0.026 μg m^{-3} for low volume samples (38.33 L min^{-1}, 24 h). The iron contamination of blank filters accounts for 0.3% of the iron on the SH_Dec2014 sample and 0.1% for the TR_mix1 sample. The exceptional loading of the AST_E45 sample reduces the blank filter contribution to 0.01% while for the TR_mix2 sample, which shows a lower aerosol loading and iron content, the filter contribution is 15% of the total iron. The blank filters were also tested at the synchrotron light source revealing negligible effects both in the XANES and in the EXAFS spectral regions.

Table 1. Summary of samples analyzed in this work: total aerosol mass concentration and Iron concentration.

Sample	Size Fraction	PM [$\mu g\ m^{-3}$]	Fe [$\mu g\ m^{-3}$]	Fe [%ww]
SH_Dec2014	PM_{10}	86.9	1.55	1.8%
TR_mix1	PM_{10}	109.9	2.30	2.1%
TR_mix2	$PM_{2.5}$	62.2	0.17	0.3%
AST_E45	TSP	1.71×10^3	230.4	13.5%

2.3. X-ray Absorption Spectroscopy

XANES and EXAFS spectra at the Fe K-edge (7112 eV) were collected at the European Synchrotron Radiation Facility (ESRF) of Grenoble, France at the LISA (formerly GILDA) CRG beamline (BM08; [42]). The beamline is equipped with a sagittally focusing monochromator using Si(311) crystals, a pair of Pd-coated mirrors (Ecutoff = 18 keV) for harmonic rejection and beam focusing, and a 12 elements Ge detector. The XAS spectra were recorded between about 6900 and 7700 eV, and a reference sample spectrum (metallic Fe foil) was collected at the same time of each sample scan to provide a reliable energy calibration. Three scans per sample were averaged to improve the signal to noise ratio, and the total measurement of a typical sample lasted about 6 h. However, no evidence of beam damage was found since the first and the last spectrum did not show any differences. The beam size of 0.5×2.0 mm ensures representative bulk analysis and not single particle measurements. Because of the low concentration of iron in the samples, we decided to work in fluorescence mode. The possibility of suffering from self-absorption phenomena has been investigated comparing the k-space data of the samples recorded in fluorescence and transmission mode. As an example, the fluorescence and transmission spectra for the sample with the highest Fe concentration (AST_E45) are reported in Figure S3 (Supplementary Material), showing no amplitude distortion that can be attributed to self-absorption.

EXAFS data analysis was performed using specific codes (Athena and Artemis; [43]).

2.4. Selective Leaching Experiments

The selective solubility of iron was studied by applying the sequential extraction scheme proposed by the European Community Bureau of Reference [44]. The method, originally developed for soil and sediment samples, was also applied to the sequential chemical fractionation of atmospheric aerosols, as reviewed by Smichowski et al. [45]. The BCR procedure consists of three sequential steps. In the first step (which releases the acid-labile fraction, i.e., carbonates and labile organic matter), sub-samples were treated with 10 mL of 0.11 M acetic acid (pH 2.8 ± 0.1), shaken for 16 h at room temperature and centrifuged for 10 min at 5000 rpm. Supernatants were then transferred into graduated flasks, acidified to 1% with (concentrated) nitric acid and stored at +4 °C until analysis. In the second step (which releases the reducible fraction, i.e., Mn and Fe oxides), 10 mL of 0.5 M hydroxylamine hydrochloride (pH 1.5 ± 0.2) were added to the residues of the previous step (after washing the residues with 4 mL of ultrapure water) and the same shaking/centrifugation/acidification procedure as in the first step was performed. Finally, in the third step (which releases the oxidizable phases, i.e., organic matter and sulfides), the residues were treated with 6.25 mL of 30% hydrogen peroxide (pH 2.5 ± 0.5), introduced into the microwave digestion system (MARS-5 by CEM, Matthews, NC, USA) and heated to 50 °C (ramp: 15 min; hold: 60 min). At the end of this step, 6.25 mL of 2 M ammonium acetate (pH 2.0 ± 0.1) were added to prevent re-adsorption processes and treated for 60 min in an ultrasonic bath (45 kHz, 130 W). Then, solutions were acidified to 1% with (concentrated) nitric acid and stored at +4 °C until analysis. In addition to the three steps of the BCR procedure, the residual fraction (silicates, aluminosilicates) was also determined by dissolving the residues of the previous steps in 6 mL of an HNO_3:HCl:HF 1:3:2 (*v/v*) mixture. Microwave-assisted digestion was conducted at 200 °C (ramp: 20 min; hold: 30 min). After cooling, 14 mL of saturated boric acid solution were added and heated again to 170 °C (ramp: 15 min; hold: 10 min). All the solutions

obtained by the sequential extraction procedure were finally analyzed by inductively coupled plasma atomic emission spectrometry (Vista PRO by Agilent Technologies, Santa Clara, CA, USA), using online internal standardization (Lu 291.139 nm) and measuring the emission intensity at selected wavelengths: (Fe 234.350, 240.489, 259.837 nm). All reagents were of analytical or, whenever available, suprapure grade quality from Merck (Darmstadt, Germany). Ultrapure water was supplied by the Milli-Q system, fed by the Elix 3 reverse osmosis system, both from Merck-Millipore (Darmstadt, Germany). Standard solutions for calibration were prepared from 1000 mg/L single-element standard solutions by Merck. The accuracy of the analytical procedures was validated with certified reference materials BCR 701 (European Community Bureau of Reference), PACS-2, MESS-2 (National Research Council Canada) and MURST-ISS-A1 (PNRA-Istituto Superiore di Sanitá, Rome).

3. Results

3.1. X-ray Absorption Spectroscopy (XAS) Results

XANES and EXAFS spectra are shown in Figures 1 and 2 for a direct comparison of the SH_Dec2014 and the AST_E45 cases. Remarkable differences are evident even at a qualitative level. The spectra of the two mixed urban samples (TR_mix1 and TR_mix2) are also shown in the same figures for comparison purpose and they show similar spectral features to Saharan dust and steel production emissions, respectively.

The fitting of the pre-edge features in the XANES part of the normalized spectrum allowed us to determine the centroid position and intensity parameters, and the results are reported in Table 2.

Table 2. XANES: pre-edge peak quantitative data analysis results on Saharan dust (SH_Dec2014), Steel production emission (AST_E45) and mixed aerosol samples collected in the Terni urban area (TR_mix1 and TR_mix2).

Sample	Centroid [eV]	Intensity
SH_Dec2014	7114.9	0.04
TR_mix1	7115.0	0.05
TR_mix2	7114.5	0.09
AST_E45	7114.2	0.09

A comparison between the pre-edge peak fit parameters for samples and standard compounds is reported in Figure 3. The centroid position suggests the presence of Fe^{3+} in Saharan dust (SH_Dec2014), steel production (AST_E45) and mixed (TR_mix1 and TR_mix2) samples, while the intensity results different for Saharan dust and steel production samples, suggesting 6-fold coordination for the first one and lower coordination for the latter. As shown in Figure 1, the shape of the pre-edge features is noticeably different for the Saharan dust and the steel production emission samples. In the first case, the peak is broad and can be fitted with two components while in the AST case it is a single peak. The broad, double peak of the Saharan dust sample can be attributed to octahedral Fe^{3+} in iron-silicate and/or iron-oxide structures. On the other hand, the intense single peak observed for the AST_E45 sample, can be attributed to the dominance of the Fe^{3+} tetrahedral sites which suggests the presence of a spinel-type structure.

For the SH_Dec2014 sample, the fit parameters (centroid = 7114.9 eV, intensity = 0.04) are compatible with those found by Wilke et al. [46] for octahedral coordinated Fe^{3+} which is characterized by the centroid position at 7114.4 eV and an intensity of about 0.12. It is worthwhile noting that these values have been rescaled as suggested by Giuli et al. [47] because our energy calibration of the Fe K-edge, accordingly to the edge position data by Bearden and Burr 1967 [48], is about 1 eV higher than the calibration value used by Wilke et al. [46]. These results are compatible with Saharan dust, mainly constituted by oxidized phases like Fe^{3+} oxy(hydr)oxides such as ferrihydrite and sheet minerals of the illite group [47,49]. As regards the E45 sample, the centroid position (7114.2eV) is quite close to

that of the Saharan sample but the intensity is higher (0.09). These results are more similar to those obtained by d'Acapito et al. [22] for an urban particulate matter, which shows a centroid position of about 7114.1 eV and an intensity around 0.18.

A direct comparison of the AST_E45 with magnetite and maghemite XANES spectra is shown in Figure S4 of the Supplementary Material. These two standards have been chosen on the basis of X-ray diffraction (XRD) results, which suggests the presence of two spinel-like phases with different unit cells, one of those compatible with magnetite, and the other compatible with maghemite or trevorite. The XANES spectrum of the sample result more similar to that of the maghemite standard, suggesting the presence of a weathered or oxidized magnetite-like structure.

As shown, the XANES region provides information on coordination and valence state of iron and, despite the centroid position and intensity values are not different enough to offer a specific fingerprint of the different iron-bearing aerosols, the shape of the pre-edge features is an indication for discriminating between the two sources that are the subject of this study.
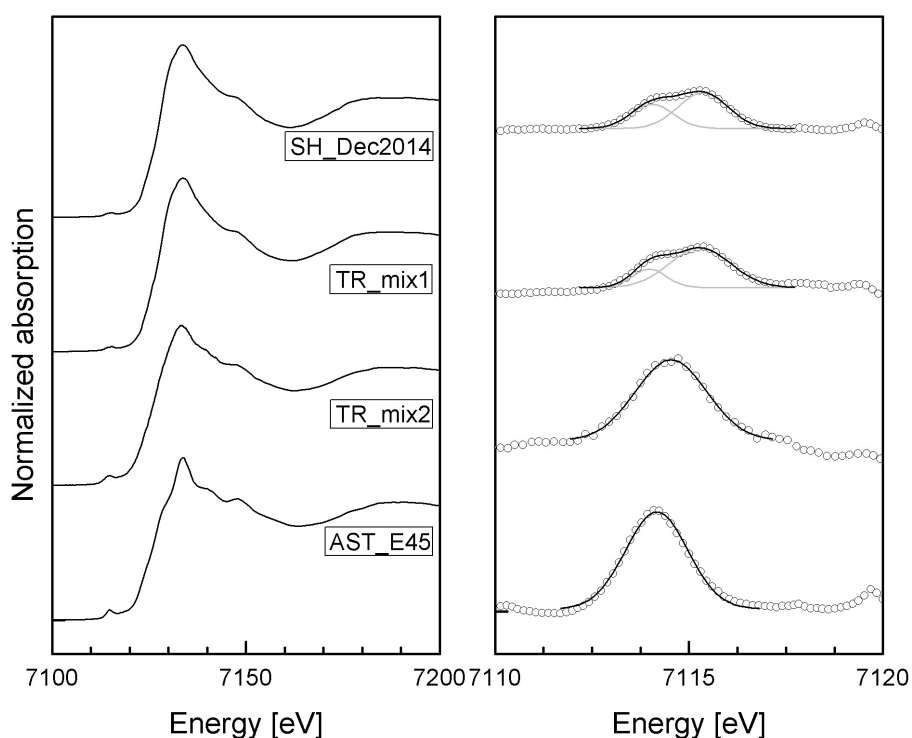

Figure 1. (**Lefthand panel**) XANES spectra of the Saharan dust (SH_Dec2014), steel production fumes (AST_E45) and mixed aerosol samples collected in the Terni urban area (TR_mix1 and TR_mix2). (**Righthand panel**) Blow-up of the pre-edge features of the same samples is shown in the lefthand panel. Here the open circles are the experimental points and the lines the model best fits (see text).

The EXAFS spectrum of the SH_Dec2014 sample was fitted with a two-shell ferrihydrite model and the results are shown in Table 3 and in Figure 2. The first shell fit gives a Fe-O distance of 1.99 ± 0.01 Å that agrees with the one calculated using the bond-valence method (BVM; [50]) for 6-coordinated Fe^{3+} (2.015 Å; Table S1), while the Fe-Fe distance is about 2.98 ± 0.01 Å. These results, obtained from the analysis of the MM PM_{10} sample of 1 December 2014, are consistent for all the samples collected on both days, on both sites (MM and Terni) and on all the different filter types during the Saharan dust event occurring in December 2014 (e.g., TR_mixSH in Table 2, r(Fe-O) = 2.01 ± 0.01 Å) This evidence demonstrates the absolute dominance of Saharan dust over local contributions. Concerning the coordination number, we obtained a local structure constituted by six oxygen atoms and two iron atoms (Table 3) compatible with the XANES observations and EXAFS bond distances.
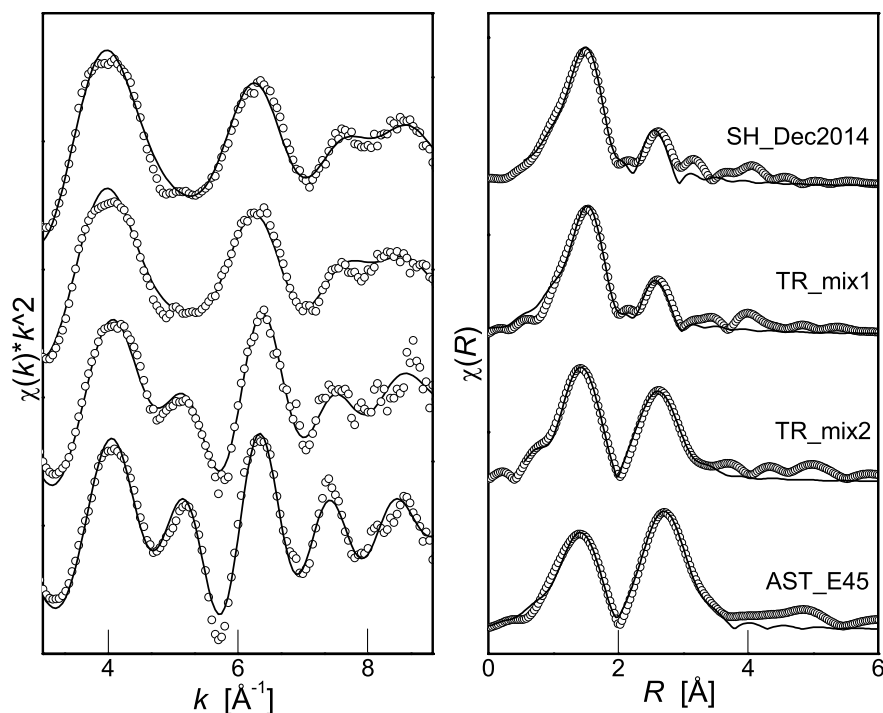
Figure 2. (**Lefthand panel**) k^2 weighted EXAFS spectra and (**Righthand panel**) the related Fourier transforms for Saharan dust (SH_Dec2014), steel production fumes (AST_E45) and mixed aerosol samples collected in the Terni urban area (TR_mix1 and TR_mix2). The open circles are the experimental data and the continuous lines the model best fits.
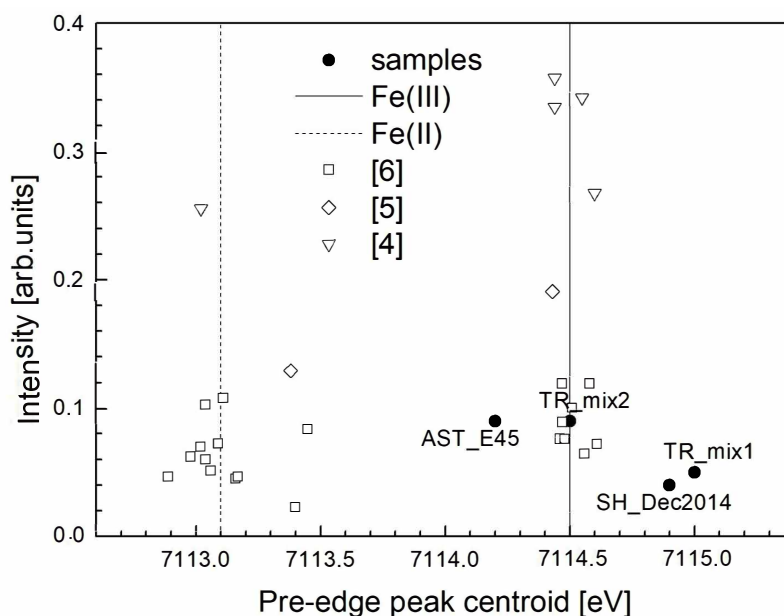

Figure 3. Pre-edge peak intensity vs. centroid position. Comparison between samples (SH_Dec2014, AST_E45, TR_mix1 and TR_mix2; solid dots) and the standard compounds reported in Wilke et al. [46] (open symbols).

For the AST_E45 sample, the fit of the oscillating part of the spectrum was performed using a magnetite model and both the octahedral and tetrahedral theoretical paths have been implemented to determine the different coordination and bond distances for Fe in the two sites. Results are shown in Table 3 and in Figure 2. The good quality of the fit proves that steel production plants emit mainly

spinel-type iron oxides. As regards Fe-O bond distances, we obtained 2.06 ± 0.06 and 1.93 ± 0.02 Å for the octahedral and tetrahedral sites, respectively; these values agree with those calculated with the BVM method (Table S1) for octahedrally coordinated Fe^{3+} (2.015 Å), and tetrahedrally coordinated Fe^{3+} (1.865 Å), respectively. Fe-Fe bond distances range between 2.98 ± 0.02 and 3.50 ± 0.02 Å for the octahedral and tetrahedral sites, respectively. The absence of Fe^{2+} observed in both XANES and EXAFS results can be explained taking into account other metals concentration in the sample. In particular, Zn concentration resulted quite high, accounting for 25.1% of Fe concentration. This piece of information suggests the presence of a prevalent direct Fe-Zn spinel [51] with Zn^{2+} balancing the overall charge.

The SH_Dec2014 and AST_E45 cases show different features in the EXAFS spectra that also determine different bond distance values for both the first and second shell. Moreover, when comparing these results with the literature ones, we noticed that the urban aerosols studied by d'Acapito et al. [22] shows very similar values to our Saharan dust sample in the first Fe-O shell (1.92–2.04 Å), while the Fe-Fe bond distance is higher for the urban sample (3.01–3.45 Å) with respect to the present desert dust aerosol sample. While in urban aerosols the dominating phase for iron is ferrihydrite, Saharan dust contains not only Fe oxy(hydr)oxides but also aluminosilicates where the six oxygen atoms in octahedral geometry are maintained but neighboring iron atoms could exhibit different distances.

Table 3. EXAFS: quantitative data analysis results for Saharan dust (SH_Dec2014), Steel production emission (AST_E45) and mixed aerosol samples collected in the Terni urban area (TR_mix1 and TR_mix2). Errors in the last significant figure are indicated in brackets.

	Fe-O			Fe-Fe		
Sample	**r(Fe-O) [Å]**	**N**	σ^2 **[Å^2]**	**r(Fe-Fe) [Å]**	**N**	σ^2 **[Å^2]**
SH_Dec2014	1.99(1)	6.5(4)	0.011(3)	2.98(1)	1.4(4)	0.01(1)
TR_mix1	2.01(1)	5.0(3)	0.009(2)	2.99(1)	1.8(4)	0.009(6)
TR_mix2^o	2.06(6)	2.4(1)	0.02(1)	2.96(1)	2.4(1)	0.02(1)
TR_mix2^t	1.94(1)	2.4(1)	0.003(1)	3.48(1)	7.1(1)	0.003(1)
AST_E45^o	2.06(6)	3.0(2)	0.03(2)	2.98(2)	3.0(2)	0.03(2)
AST_E45^t	1.93(2)	1.9(2)	0.003(5)	3.50(2)	5.8(2)	0.003(5)

Legend: o: octahedral site, *t*: tetrahedral site.

3.2. Leaching Tests Results

Leaching tests performed on three samples (Table 4) show a general predominance of the insoluble residual fraction above the others. However, a significant difference is evident between the SH_Dec2014 and AST_E45 samples: for Saharan dust, the residual fraction accounts for 69% of total iron while in steel production emission it accounts for 93%. According to XAS results, the residual fraction of SH_Dec2014 may be ascribed to aluminosilicates and iron oxy(hydr)oxides, whereas the AST_E45 residue is attributable to spinel-type non-reducible iron oxides. In fact, well-crystalline (e.g., hematite and goethite) and short-range-ordered (e.g., ferrihydrite) iron oxides could be not completely extracted by hydroxylamine hydrochloride - depending on the sample type, the sample mass/solution volume ratio, and the reagent concentration [52,53] and hence remain in the residual fraction.

These results agree with Sammut et al. [32] who observed a residual iron phase that accounted for more than 90% in steel plant emissions and attributed it to insoluble iron oxides. Dabek-Zlotorzynska et al. [54] applied the BCR sequential leaching extraction procedure to samples of the certified NIST-1648-PM urban aerosols and showed that the refractory fraction accounts for about 80% of total iron. Moreover, the iron distribution determination performed by the authors [54] using of Mössbauer spectroscopy revealed that the refractory fraction consists mainly of magnetite, hematite and ferric/ferrous species contained in clay minerals. The TR_mix1 sample shows intermediate values between the two above cases, probably due to the external and internal mixing and atmospheric processing.

Table 4. Leaching test results on Saharan dust (SH_Dec2014), steel production emission (AST_E45) and mixed Saharan (TR_mix1) samples.

Sample	I (%)	II (%)	III (%)	IV (%)	tot Fe (µg)
SH_Dec2014	15	8	8	69	21.2
AST_E45	4	2	1	93	308.0
TR_mix1	11	6	5	78	37.6

Legend: I step: acid-labile fraction, II step: reducible Fe oxides and hydroxides, III step: oxidizable phase, IV step: insoluble residuals.

4. Discussion

This section summarizes the results obtained for the two specific aerosol types and illustrates an application to two mixed cases, namely urban aerosol contaminated by a Saharan dust advection and urban aerosol collected near the steel plant.

4.1. Saharan Dust

Saharan dust advections are typically associated with a significant increase of the total iron concentration in the aerosols [13]. In our long-term measurements started in 2009 [35] we observed that Saharan dust events recorded at MM are always associated with a high increase in the total iron concentration together with an increase in the concentrations of other metals such as Mn, Ti, and Ca. Saharan dust is mainly constituted by aluminosilicates and quartz with variable contributions of carbonates and metal oxides and hydroxides [55,56]. Interestingly, in a recent work, Formenti et al. [28] demonstrated that, in African dust, goethite is predominant over hematite.

The pure Saharan dust advection of 30 November–1 December 2014 is characterized by 6-fold coordinated Fe^{3+}. The oxidation state and coordination number are compatible with both aluminosilicates such as illite [49] and iron oxy(hydr)oxides [22]. Moreover, ferrihydrite is the most soluble among the iron oxy(hydr)oxides and thus can play an important role on iron solubility and bioavailability [57]. The presence of oxy(hydr)oxide phases in the Saharan dust has already been demonstrated and recognized in the literature [27], and increasing amounts of ferrihydrite have been found for increasing extent of long-range transport [58]. This occurrence is compatible with the ageing of dust by cloud chemistry processes, as the low pH promotes the removal and oxidation of Fe^{2+} contained in silicates [29].

Scanning Electron Microscopy (SEM) morphological and compositional analyses of the aerosol particles collected during the Saharan dust advection of December 2014, reported in Supplementary Material Figure S5, show the predominance of silicates with the presence of small amounts of Fe oxi(hydr)oxides nanoparticles which are included in the clay minerals, supporting XAS observations.

Regarding the solubility of the Saharan dust sample, we observed that the insoluble residual fraction is dominating over the others. Journet et al. [10] have demonstrated that, although the iron content is far much higher in iron oxy(hydr)oxides, the solubility of iron in mineral dust is mainly due to aluminosilicates such as clays or feldspars. The two items of evidence lead to a potentially high iron solubility for desert dust samples. These results are significant in the solubility and bioavailability context because Saharan dust is shown to have a higher percentage of soluble iron, which enhances its capacity of interaction with the hydrological cycle (CCN capacity) and the biosphere, both on ecosystems and health issues.

4.2. Steel Production Emissions

Steel production plants emit mainly submicrometric particles of metal oxides [59,60]. Previous observations by Moroni et al. [39] on aerosol samples collected at a variable height over the city of Terni, by tethered balloon experiments, and analyzed using SEM revealed the presence of metal oxides in the TK-AST emissions. Both XANES and EXAFS results point towards spinel-like structures containing Fe^{3+} in octahedral and tetrahedral sites, and, most probably, Zn^{2+} for charge balance. This

suggests that the extremely high concentration of iron oxy(hydr)oxides found in steel plant emissions causes a limited availability of soluble iron. However, this result cannot be generalized to all the anthropogenic Fe-bearing aerosols: as shown by Moffet et al. [61], some anthropogenic aerosol sources (i.e., coal combustion) emit aerosols whose iron solubility is higher as compared to mineral dust.

Leaching tests also highlight the presence of other species such as carbonates, oxides, and sulfides, compatible with steel manufacturing processes. Oxides and sulfides, in particular, develop in the presence of trace amounts of sulfur in the welding matrices. They are considered undesirable constituents in steel as they form non-metallic inclusions which tend to worsen the mechanical properties of steel, although the addition of trace sulfur amounts tends to improve the machinability of a steel [62]. However, even if leaching test points out the presence of small quantities of other phases, the EXAFS spectrum is the result of a sum of contributions and the spinel-like one is predominant, masking the others.

To sum up, since the majority of iron is in spinel-type structures, its solubility in the steel production emissions is very low. It is worth noting, however, that we analyzed samples of freshly emitted aerosols, and that the atmospheric processing could bring about changes in composition and oxidation state. However, in some of our in-progress studies, we are demonstrating that the deposition of aerosols emitted from the steel production plant in the Terni area is very localized and decreases drastically in a few kilometers range from the emitting source.

4.3. Mixed Urban Dust Cases

The XAS spectrum of the TR_mix1 sample is very similar to the one of the sample collected at MM on the same day both in the XANES (Figure 1) and in the EXAFS (Figure 2) regions, demonstrating the apparent dominance of the Saharan contribution over other local contributions in determining the observed spectral features. The leaching test on the TR_mix1 sample, on the other hand, shows a modification in the leaching stages of the urban sample with respect to the pure Saharan dust sampled at MM (Table 4). Moreover, iron concentration is higher in the urban mixed case (Table 1), suggesting other Fe-bearing aerosol sources to contribute to the overall iron concentration. Besides the steel production emissions and the Saharan dust, the remaining airborne iron mass in Terni is influenced by some other natural and anthropogenic sources such as auto vehicular traffic emissions, road dust, biomass burning, and residential heating [36,39]. These observations also suggest that the Saharan dust entrainment process into the urban boundary layer affected the iron concentration and properties, due to the mixing with the urban aerosols, while affects both the observed iron local structure and the overall solubility.

The TR_mix2 sample, on the other hand, shows spectral features similar to the pure steel plant emission case both in the XANES and in the EXAFS region (Figures 1 and 2). However, some differences between the two samples are observed. In particular, the shift of the pre-edge features at higher energy values suggest a higher octahedral Fe^{3+} content with respect to freshly emitted steel plant fumes. These observations emphasize the role of atmospheric processing and external mixing with other Fe-bearing aerosol sources of the steel plant fumes in the urban environment.

5. Conclusions

In this work, we assessed iron speciation and local structure for two well-characterized atmospheric aerosol types, namely Saharan dust and steel production plant emissions. The synergistic approach applied to combine selective leaching experiments with XAS analyses allowed us to distinguish the two cases clearly. In particular, Saharan dust result mainly constituted by aluminosilicates and iron oxy(hydr)oxides which account for 69% of the total iron content. The pre-edge feature in the XANES spectrum is a broad double peak, and the bond distances obtained from the fit of the EXAFS spectrum agree with 6-fold coordinated Fe^{3+}. For steel production emissions, the presence of spinel-like oxide phases, which has also been evidenced by XRD, accounts for 93% of total iron in the residual insoluble fraction. We considered, in the EXAFS fit, the presence of tetrahedral Fe^{3+}

shapes the pre-edge feature in a single peak, and both the tetrahedral and octahedral sites. Speciation analysis evidence the dominance of Fe^{3+} in both sites, and the elevated concentration of Zinc support this hypothesis since this element can balance the charge in the defective spinel structure. The two mixed cases showed very similar spectral shapes to the corresponding pure cases, while we noticed differences at a quantitative level. Therefore, the applied experimental approach has proved to be a useful tool in distinguishing natural and anthropogenic Fe-bearing aerosols and has the potential to be applied to other mixed cases.

Supplementary Materials: The following are available online at http://www.mdpi.com/2073-4433/10/1/8/s1, Figure S1: Sampling sites maps, Figure S2: Saharan dust advection, Figure S3: Self-absorption, Figure S4: AST_E45 sample comparison with model spinels, Table S1: Bond-Valence Method calculations, Figure S5: SEM-EDX analysis of the Saharan dust sample.

Abbreviations

The following abbreviations are used in this manuscript:

XAS	X-ray Absorption Spectroscopy
XANES	X-ray Absorption Near Edge Structure
EXAFS	Extended X-ray Absorption Fine Structure
ICP-OES	Inductively Coupled Plasma - Optical Emission Spectroscopy
EMEP	European Monitoring and Evaluation Program
TK-AST	ThyssenKrupp Acciai Speciali Terni
MM	Monte Martano
WMO SDS-WAS	World Meteorological Organization Sand and Dust Storms - Warning Advisory and Assessment System
SDO	Saharan Dust Outbreak
BTs	Back Trajectories
HVS	High-Volume Sampler
ESRF	European Synchrotron Radiation Facility
LISA	Linea Italiana di Spettroscopia di Assorbimento a raggi-X
CRG	Collaborating Research Group

References

1. Jickells, T.; An, A.; Andersen, K.; Baker, A.; Bergametti, G.; Brooks, N.; Cao, J.; Boyd, P.; Duce, R.; Hunter, K.; et al. Global iron connections between desert dust, ocean biogeochemistry, and climate. *Science* **2005**, *308*, 67–71. [CrossRef] [PubMed]
2. Ben-Ami, Y.; Koren, I.; Rudich, Y.; Artaxo, P.; Martin, S.; Andreae, M. Transport of North African dust from the Bodélé depression to the Amazon Basin: A case study. *Atmos. Chem. Phys.* **2010**, *10*, 7533–7544. [CrossRef]
3. Abouchami, W.; Nathe, K.; Kumar, A.; Galer, S.; Jochum, K.; Williams, E.; Horbe, A.; Rosa, J.; Balsam, W.; Adams, D.; et al. Geochemical and isotopic characterization of the Bodélé Depression dust source and implications for transatlantic dust transport to the Amazonian Basin. *Earth Planet. Sci. Lett.* **2013**, *380*, 112–123. [CrossRef]

4. Smetacek, V.; Klaas, C.; Strass, V.; Assmy, P.; Montresor, M.; Cisewski, B.; Savoye, N.; Webb, A.; d'Ovidio, F.; Arrieta, J.; et al. Deep carbon export from a Southern Ocean iron-fertilized diatom bloom. *Nature* **2012**, *487*, 313–319. [CrossRef]

5. Stafoggia, M.; Zauli-Sajani, S.; Pey, J.; Samoli, E.; Alessandrini, E.; Basagana, X.; Cernigliaro, A.; Chiusolo, M.; Demaria, M.; Dìaz, J.; et al. Desert dust outbreaks in Southern Europe: Contribution to daily PM$_{10}$ concentrations and short-term associations with mortality and hospital admissions. *Environ. Health Perspect.* **2015**. [CrossRef] [PubMed]

6. Dall'Osto, M.; Booth, M.; Smith, W.; Fisher, R.; Harrison, R. A study of the size distributions and the chemical characterization of airborne particles in the vicinity of a large integrated steelworks. *Aerosol Sci. Technol.* **2008**, *42*, 981–991. [CrossRef]

7. Hedberg, Y.; Gustafsson, J.; Karlsson, H.; Moller, L.; Wallinder, I. Bioaccessibility, bioavailability and toxicity of commercially relevant iron- and chromium-based particles: In vitro studies with an inhalation perspective. *Part. Fibre Toxicol.* **2010**, *7*. [CrossRef]

8. Smith, K.; Aust, A. Mobilization of iron from urban particulates leads to generation of reactive oxygen species in vitro and induction of ferritin synthesis in human lung epithelial cells. *Chem. Res. Toxicol.* **1997**, *10*, 828–834. [CrossRef]

9. Schroth, A.; Crusius, J.; Sholkovitz, E.; Bostick, B. Iron solubility driven by speciation in dust sources to the ocean. *Nat. Geosci.* **2009**, *2*, 337–340. [CrossRef]

10. Journet, E.; Desboeufs, K.; Caquineau, S.; Colin, J. Mineralogy as a critical factor of dust iron solubility. *Geophys. Res. Lett.* **2008**, *35*. [CrossRef]

11. Baker, A.; Jickells, T. Mineral particle size as a control on aerosol iron solubility. *Geophys. Res. Lett.* **2006**, *33*. [CrossRef]

12. Shi, Z.; Krom, M.; Jickells, T.; Bonneville, S.; Carslaw, K.; Mihalopoulos, N.; Baker, A.; Benning, L. Impacts on iron solubility in the mineral dust by processes in the source region and the atmosphere: A review. *Aeolian Res.* **2012**, *5*, 21–42. [CrossRef]

13. Mahowald, N.; Baker, A.; Bergametti, G.; Brooks, N.; Duce, R.; Jickells, T.; Kybilay, N.; Prospero, J.; Tegen, I. Atmospheric global dust cycle and iron inputs to the ocean. *Glob. Biogeochem. Cycles* **2005**, *19*. [CrossRef]

14. Majestic, B.; Schauer, J.; Shafer, M.; Turner, J.; Fine, P.; Singh, M.; Sioutas, C. Development of a wet-chemical method for the speciation of iron in atmospheric aerosols. *Environ. Sci. Technol.* **2006**, *40*, 2346–2351. [CrossRef] [PubMed]

15. Hoffmann, P.; Dedik, A.; Ensling, J.; Weinbruch, S.; Weber, S.; Sinner, T.; Gulitch, P.; Ortner, H. Speciation of iron in atmospheric aerosol samples. *J. Aerosol Sci.* **1996**, *27*, 325–337. [CrossRef]

16. Westre, T.; Kennepohl, P.; DeWitt, J.; Hedman, B.; Hodgson, K.; Solomon, E. A multiplet analysis of Fe K-edge 1s-3d pre-edge features of iron complexes. *J. Am. Chem. Soc.* **1997**, *119*, 6297–6314. [CrossRef]

17. Lee, P.; Citrin, P.; Eisenberger, P.; Kincaid, B. Extended X-ray absorption fine structure—Its strenghts and limitations as a structural tool. *Rev. Mod. Phys.* **1981**, *53*, 769–806. [CrossRef]

18. Qi, J.; Zhang, M.; Feng, L.; Li, X. An EXAFS study on the local structure around iron in atmospheric aerosols collected in the Qingdao area. *Molecules* **2003**, *8*, 31–39. [CrossRef]

19. Wang, Y.; Li, A.; Zhang, Y.; Xie, Y.; Li, D.; Zhang, G. Speciation of iron in atmospheric particulate matter by EXAFS. *Chin. Sci. Bull.* **2006**, *51*, 2275–2280. [CrossRef]

20. Elzinga, E.; Gao, Y.; Fitts, J.; Tappero, R. Iron speciation in urban dust. *Atmos. Environ.* **2011**, *45*, 4528–4532. [CrossRef]

21. Oakes, M.; Weber, R.; Lai, B.; Russell, A.; Ingall, E. Characterization of iron speciation in urban and rural single particles using XANES spectroscopy and micro X-ray fluorescence measurements: Investigating the relationships between speciation and fractional iron solubility. *Atmos. Chem. Phys.* **2012**, *12*, 745–756. [CrossRef]

22. d'Acapito, F.; Tagliani, S.M.; Benedetto, F.D.; Gianfagna, A. Local order and valence state of Fe in urban suspended particulate matter. *Atmos. Environ.* **2014**, *99*, 582–586. [CrossRef]

23. Valotto, G.; Cattaruzza, E.; Bardelli, F. Multi-edge X-ray absorption spectroscopy study of road dust samples from a traffic area of Venice using stoichiometric and environmental references. *Spectrochim. Acta Part A Mol. Biomol. Spectrosc.* **2017**, *173*, 971–978. [CrossRef] [PubMed]

24. Marcelli, A.; Hampai, D.; Giannone, F.; Sala, M.; Maggi, V.; Marino, F.; Pignotti, S.; Cibin, G. XRF-XANES characterization of deep ice core insoluble dust. *J. Anal. At. Spectrosc.* **2012**, *27*, 33–37. [CrossRef]

25. Baccolo, G.; Cibin, G.; Delmonte, B.; Hampai, D.; Marcelli, A.; Stefano, E.D.; Macis, S.; Maggi, V. The contribution of synchrotron light for the characterization of atmospheric mineral dust in deep ice cores: Preliminary results from the Talos Dome ice core (East Antarctica). *Condens. Matter* **2018**, *3*, 25. [CrossRef]

26. Lazaro, F.; Gutierrez, L.; Barron, V.; Gelado, M. The speciation of iron in desert dust collected in Gran Canaria (Canary Islands): Combined chemical, magnetic and optical analysis. *Atmos. Environ.* **2008**, *42*, 8987–8996. [CrossRef]

27. Deboudt, K.; Gloter, A.; Mussi, A.; Flament, P. Red-ox speciation and mixing state of iron in individual African dust particles. *J. Geophys. Res.* **2012**, *117*. [CrossRef]

28. Formenti, P.; Caquineau, S.; Chevaillier, S.; Klaver, A.; Desboeufs, K.; Rajot, J.; Belin, S.; Briois, V. Dominance of goethite over hematite in iron oxides of mineral dust from Western Africa: Quantitative partitioning by X-ray absorption spectroscopy. *J. Geophys. Res. Atmos.* **2014**, *119*, 12740–12754. [CrossRef]

29. Nickovic, S.; Vukovic, A.; Vujadinovic, M. Atmospheric processing of iron carried by mineral dust. *Atmos. Chem. Phys.* **2013**, *13*, 9169–9181. [CrossRef]

30. Shi, Z.; Krom, M.; Bonneville, S.; Baker, A.; Bristow, C.; Drake, N.; Mann, G.; Carslaw, K.; McQuaid, J.; Jickells, T.; Benning, L. Influence of chemical weathering and aging of iron oxides on the potential iron solubility of Saharan dust during simulated atmospheric processing. *Glob. Biogeochem. Cycles* **2011**, *25*. [CrossRef]

31. Majestic, B.; Schauer, J.; Shafer, M. Application of synchrotron radiation for measurement of iron red-ox speciation in atmospherically processed aerosols. *Atmos. Chem. Phys.* **2007**, *7*, 2475–2487. [CrossRef]

32. Sammut, M.; Noack, Y.; Rose, J. Zinc speciation in steel plant atmospheric emissions: A multi-technical approach. *J. Geochem. Explor.* **2006**, *88*, 239–242. [CrossRef]

33. Sammut, M.; Noack, Y.; Rose, J.; Hazemann, J.; Proux, O.; Depoux, M.; Ziebel, A.; Fiani, E. Speciation of Cd and Pb in dust emitted from sinter plant. *Chemosphere* **2010**, *78*, 445–450. [CrossRef] [PubMed]

34. Marris, H.; Deboudt, K.; Flament, P.; Grobety, B.; Giere, R. Fe and Mn oxidation states by TEM-EELS in fine-particle emissions from a Fe-Mn alloy making plant. *Environ. Sci. Technol.* **2013**, *47*, 10832–10840. [CrossRef] [PubMed]

35. Moroni, B.; Castellini, S.; Crocchianti, S.; Piazzalunga, A.; Fermo, P.; Scardazza, F.; Cappelletti, D. Ground-based measurements of long-range transported aerosol at the rural regional background site of Monte Martano (Central Italy). *Atmos. Res.* **2015**, *155*, 26–36. [CrossRef]

36. Moroni, B.; Cappelletti, D.; Marmottini, F.; Scardazza, F.; Ferrero, L.; Bolzacchini, E. Integrated single particle-bulk chemical approach for the characterization of local and long range sources of particulate pollutants. *Atmos. Environ.* **2012**, *50*, 267–277. [CrossRef]

37. Federici, E.; Petroselli, C.; Montalbani, E.; Casagrande, C.; Ceci, E.; Moroni, B.; Porta, G.L.; Castellini, S.; Selvaggi, R.; Sebastiani, B.; et al. Airborne bacteria and persistent organic pollutants associated with an intense Saharan dust event in the Central Mediterranean. *Sci. Total Environ.* **2018**, *645*, 401–410. [CrossRef]

38. Petroselli, C.; Crocchianti, S.; Moroni, B.; Castellini, S.; Selvaggi, R.; Nava, S.; Calzolai, G.; Lucarelli, F.; Cappelletti, D. Disentangling the major source areas for an intense aerosol advection in the Central Mediterranean on the basis of Potential Source Contribution Function modeling of chemical and size distribution measurements. *Atmos. Res.* **2018**, *204*, 67–77. [CrossRef]

39. Moroni, B.; Ferrero, L.; Crocchianti, S.; Perrone, S.; Sangiorgi, M.; Bolzacchini, E.; Cappelletti, D. Aerosol dynamics upon Terni basin (Central Italy): Results of integrated vertical profile measurements and electron microscopy analyses. *Rendiconti Lincei* **2013**, *24*, 319–328. [CrossRef]

40. Draxler, R.; Rolph, G. HYSPLIT (HYbrid Single-Particle Lagrangian Integrated Trajectory) Model Access via NOAA ARL READY. 2012. Available online: http://ready.arl.noaa.gov/HYSPLIT.php (accessed on 29 December 2018).

41. Escudero, M.; Querol, X.; Pey, J.; Alastuey, A.; Perez, N.; Ferreira, F.; Alonso, S.; Rodriguez, S.; Cuevas, E. A methodology for the quantification of the net African dust load in air quality monitoring networks. *Atmos. Environ.* **2007**, *41*, 5516–5524. [CrossRef]

42. d'Acapito, F.; Trapananti, A.; Torrengo, S.; Mobilio, S. X-ray Absorption Spectroscopy: The Italian beamline GILDA of the ESRF. *Notiziario Neutroni e Luce di Sincrotrone* **2014**, *19*, 14–23.

43. Ravel, B.; Newville, M. ATHENA, ARTEMIS, HEPHAESTUS: Data analysis for X-ray absorption spectroscopy using IFEFFIT. *J. Synchrotron Radiat.* **2005**, *12*, 537–541. [CrossRef] [PubMed]

44. Pueyo, M.; Rauret, G.; Lück, D.; Yli-Halla, M.; Muntau, H.; Quevauviller, P.; Lopez-Sanchez, J. Certification of the extractable contents of Cd, Cr, Cu, Ni, Pb and Zn in a freshwater sediment following a collaboratively tested and optimised three-step sequential extraction procedure. *J. Environ. Monit.* **2001**, *3*, 243–250. [CrossRef] [PubMed]

45. Smichowski, P.; Polla, G.; Gomez, D. Metal fractionation of atmospheric aerosols via sequential chemical extraction: A review. *Anal. Bioanal. Chem.* **2005**, *381*, 302–316. [CrossRef]

46. Wilke, M.; Farges, F.; Petit, P.; Brown, G.; Martin, F. Oxidation state and coordination of Fe in minerals: An Fe K-XANES spectroscopic study. *Am. Mineral.* **2001**, *86*, 714–730. [CrossRef]

47. Giuli, G.; Pratesi, G.; Cipriani, C.; Paris, E. Iron local structure in tektites and impact glasses by extended X-ray absorption fine structure and high-resolution X-ray absorption near-edge structure spectroscopy. *Geochim. Cosmochim. Acta* **2002**, *66*, 4347–4353. [CrossRef]

48. Bearden, J.A.; Burr, A.F. Reevaluation of X-ray atomic energy levels. *Rev. Mod. Phys.* **1967**, *39*, 125–142. [CrossRef]

49. O'day, P.; Rivera, N.; Root, R.; Carroll, S. X-ray absorption spectroscopic study of Fe reference compounds for the analysis of natural sediments. *Am. Mineral.* **2004**, *89*, 572–585. [CrossRef]

50. Newville, M. Using Bond Valence sums as restrains in XAFS analysis. *Phys. Scr.* **2005**, *T115*, 159–161. [CrossRef]

51. Oliver, S.; Harris, V.; Hamdeh, H.H.; Ho, J.C. Large zinc cation occupancy of octahedral sites in mechanically activated zinc ferrite powders. *Appl. Phys. Lett.* **2000**, *76*, 2761–2763. [CrossRef]

52. Suda, A.; Makino, T.; Higashi, T. Extractability of manganese and iron oxides in typical Japanese soils by 0.5 mol/L hydroxylamine hydrochloride (pH 1.5). *Soil Sci. Plant Nutr.* **2012**, *58*, 684–695. [CrossRef]

53. Suda, A.; Makino, T.; Higashi, T. An improved selective extraction method for Mn oxides and occluded metals with emphasis on applicability to Andisols. *Soil Sci. Plant Nutr.* **2013**, *59*, 840–851. [CrossRef]

54. Dabek-Zlotorzynska, E.; Kelly, M.; Chen, H.; Chakrabarti, C. Evaluation of capillary electrophoresis combined with a BCR sequential extraction for determining distribution of Fe, Zn, Cu, Mn, and Cd in airborne particulate matter. *Anal. Chim. Acta* **2003**, *498*, 175–187. [CrossRef]

55. Coz, E.; Gomez-Moreno, F.; Pujadas, M.; Casuccio; G.S.; Lersch, T.; Artinano, B. Individual particle characteristics of North African dust under different long-range transport scenarios. *Atmos. Environ.* **2009**, *43*, 1850–1863. [CrossRef]

56. Scheuvens, D.; Schutz, L.; Kandler, K.; Ebert, M.; Weinbruch, S. Bulk composition of northern African dust and its source sediments—A compilation. *Earth Sci. Rev.* **2013**, *116*, 170–194. [CrossRef]

57. Hiemstra, T. Surface and mineral structure of ferrihydrite. *Geochim. Cosmochim. Acta* **2013**, *105*, 316–325. [CrossRef]

58. Takahashi, Y.; Higashi, M.; Furukawa, T.; Mitsunobu, S. Change of iron species and iron solubility in Asian dust during the long-range transport from western China to Japan. *Atmos. Chem. Phys.* **2011**, *11*, 11237–11252. [CrossRef]

59. Ebert, M.; Muler-Ebert, D.; Benker, N.; Weinbruch, S. Source apportionment of aerosol particles near a steel plant by electron microscopy. *J. Environ. Monit.* **2012**, *14*, 3257–3266. [CrossRef]

60. Arndt, J.; Deboudt, K.; Anderson, A.; Blondel, A.; Eliet, S.; Flament, P.; Fourmentin, M.; Healy, R.; Savary, V.; Setyan, A.; et al. Scanning electron microscopy-energy dispersive X-ray spectrometry (SEM-EDX) and aerosol time-of-flight mass spectrometry (ATOFMS) single particle analysis of metallurgy plant emissions. *Environ. Pollut.* **2016**, *210*, 9–17. [CrossRef]

61. Moffet, R.; Furutani, H.; Rodel, T.; Henn, T.; Sprau, P.; Laskin, A.; Uematsu, M.; Gilles, M. Iron speciation and mixing in single aerosol particles from the Asian continental outflow. *J. Geophys. Res.* **2012**, *117*. [CrossRef]

62. Anmark, N.; Karasev, A.; Jonsson, P. The effect of different non-metallic inclusions on the machinability of steels. *Materials* **2015**, *8*, 751–783. [CrossRef] [PubMed]